Medical Physics
The International Journal of Medical Physics Research and Practice

Coherent scatter in diagnostic radiology

P. C. Johns and M. J. Yaffe

Citation: Medical Physics **10**, 40 (1983); doi: 10.1118/1.595443
View online: http://dx.doi.org/10.1118/1.595443
View Table of Contents: http://scitation.aip.org/content/aapm/journal/medphys/10/1?ver=pdfcov
Published by the American Association of Physicists in Medicine

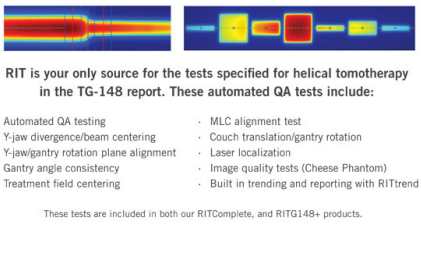

Coherent scatter in diagnostic radiology

P. C. Johns and M. J. Yaffe

Department of Medical Biophysics, University of Toronto, 500 Sherbourne Street, Toronto, Ontario, M4X1K9, Canada
and
Radiological Research Laboratories, University of Toronto, Medical Sciences Building, 1 King's College Circle, Toronto, Ontario, M5S 1A8, Canada

(Received 12 May 1982; accepted for publication 14 July 1982)

Coherent scatter is often ignored in diagnostic radiology because its cross section is relatively small, and because it is assumed to be indistinguishable from primary radiation. Single-scatter calculations, however, show that coherently scattered photons diverge sufficiently from the primary ray to degrade image contrast, and that they account for a significant fraction of the total scattered energy fluence at the image receptor. Grids and large air gaps are less effective in reducing coherent single scatter than incoherent and multiple scatter. For radiography of the abdomen, coherent first scatter comprises 10% of total scatter and 26% of the primary fluence before a grid, and on the order of 22% and 7.5%, respectively, behind a grid. Coherent first scatter comprises a higher fraction of the total amount of scatter for lower energy examinations such as mammography.

Key words: diagnostic radiology, scattered radiation, coherent scatter, x-ray diffraction

I. INTRODUCTION

In diagnostic radiology, radiation scattered by the patient degrades image quality[1] by reducing radiographic contrast and signal-to-noise ratio (SNR). Therefore, much attention has been given to developing ways to reduce the amount of scatter reaching the image receptor.

At diagnostic energies other than for mammography, the probability for coherent scattering is much less than that for incoherent (Fig. 1). For this reason, coherent scatter has received little attention in diagnostic radiology, aside from development of procedures to quantify bone mineral content.[2–4]

Unlike other interaction processes the angular dependence of coherent scatter is highly forward peaked. As will be seen, this means that the amount of coherent scatter reaching the image receptor is significant.

It has sometimes been assumed that due to its forward peaked nature, coherent scatter behaves like primary radiation, and can be neglected as an image-degrading factor. It will be shown, however, that in the geometries typically used in diagnostic radiology, coherently scattered photons diverge sufficiently from the primary path for this not to be so.

Although recent Monte Carlo simulation studies[5–7] have included coherent scatter, the coherent component has not been quantified separately. As well, the differential coherent scattering cross sections that have been used have not included the effects of interference between scatterings from electrons of different molecules. These affect the angular distribution of coherent scatter.

This paper reports the results of calculations of the magnitude and distribution of single or first-order coherent scatter. We compare these to measurements of the total amount of scatter reaching the image receptor in diagnostic imaging

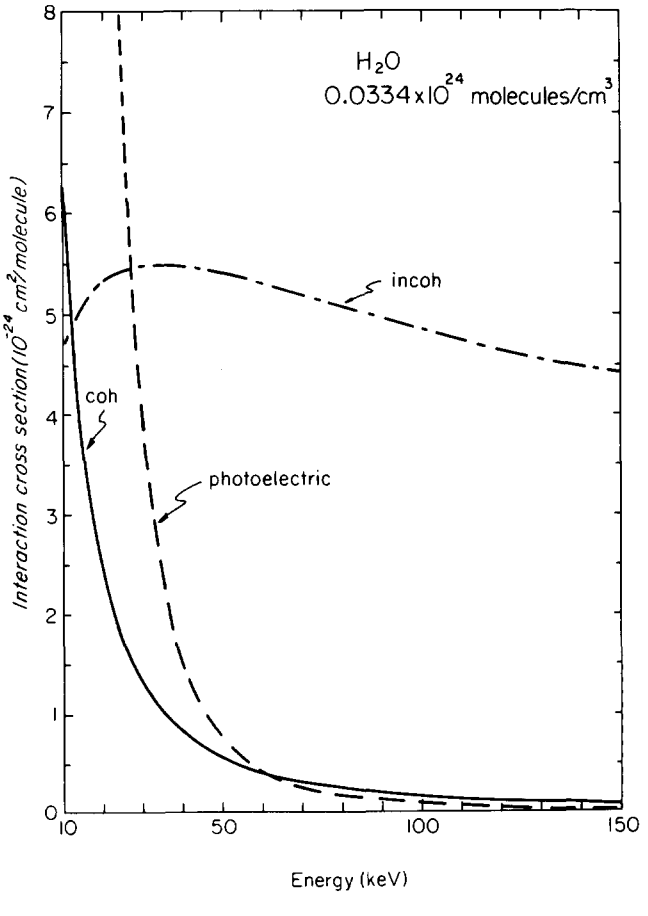

FIG. 1. Interaction cross sections for water. Coherent cross sections calculated from the diffraction data reported by Narten (Ref. 16). The incoherent cross sections are the sum of the oxygen plus twice the hydrogen cross sections given by Hubbell *et al.* (Ref. 13). Photoelectric cross sections from Plechaty *et al.* (Ref. 22).

 0094-2405/83/010040-11$01.20

geometries. Our first-scatter calculations are supported by measurements made under conditions in which single scatter predominates, allowing direct comparison between theory and experiment.

II. FIRST-SCATTER CALCULATIONS

$S_{1,\mathrm{coh}}/P$ and $S_{1,\mathrm{incoh}}/P$, the ratios of the coherent and incoherent first-order scattered energy fluences to primary, respectively, were calculated for a number of phantom geometries by dividing the volume of the phantom irradiated by primary into small elements, and summing the first-scattered fluences from each. For volume element i, the fluence of first-scattered energy per unit area in the image plane at point p is

$$S_i = P_i\left(\frac{d\sigma}{d\Omega}\right)_i \rho_{\mathrm{mol}} V_i E_i \left(\frac{d\Omega}{da}\right)_i T_{\mathrm{Si}}, \tag{1}$$

where P_i is the primary number fluence reaching i, corrected for attenuation and inverse square law, $(d\sigma/d\Omega)_i$ is the cross section per molecule per steradian for scattering from i towards p, the product $\rho_{\mathrm{mol}} V_i$ is the number of molecules in i, E_i is the energy per scattered photon, $(d\Omega/da)_i$ is the solid angle subtended at i by a unit area in the image plane at p, and T_{Si} is the transmission of the scattered fluence through the phantom material between i and p.

Primary x-ray spectra were taken from Birch *et al.*[8] For beams used in mammography, 1-keV-wide energy bins were used. For the more energetic beams, 5-keV-wide bins were employed. Single-scatter calculations were performed for each energy bin and the overall scatter-to-primary ratios were obtained by summing the individual calculations.

III. SCATTERING CROSS SECTIONS

In this work, we have used water as the phantom material. Water is the most commonly used substance for diagnostic radiological phantoms, and in the ICRP Reference Man[9] comprises 60% of the total body, and 65% of the soft tissue, by weight. For specialized examinations such as mammography, where the effect of the elevated adipose content is appreciable at the low x-ray energies used, other, more refined phantoms are appropriate.[10] The major conclusions of our work, however, are insensitive to the choice of phantom material.

In order to compare our results with the measurements of Barnes and Brezovich[11] for mammography, we have also performed scattering calculations for a Lucite phantom.

A. Coherent scattering

The differential cross section per molecule per unit solid angle for coherent or Rayleigh scattering is

$$d\sigma_{\mathrm{coh}}(\theta)/d\Omega = [F_{\mathrm{coh}}(s, \rho_e(\mathbf{r}))]^2 \, d\sigma_T(\theta)/d\Omega, \tag{2}$$

where $F_{\mathrm{coh}}(s, \rho_e(\mathbf{r}))$ is a coherent form factor which accounts for the wave interference between scatterings from different electrons, and

$$d\sigma_T(\theta)/d\Omega = \tfrac{1}{2} r_e^2 (1 + \cos^2\theta) \tag{3}$$

is the differential Thomson cross section per electron for elastic scattering of an unpolarized beam, where

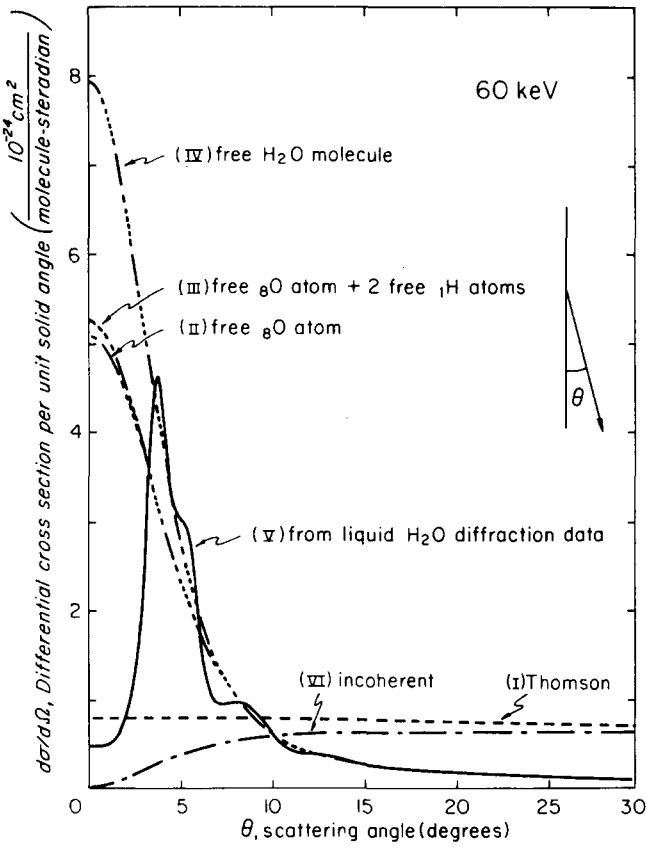

FIG. 2. Differential scattering cross sections at 60 keV from 0° to 30°. Curve (I) ten times the differential Thomson cross section per electron; (II) coherent scattering from isolated oxygen atoms (Ref. 13); (III) twice the differential coherent cross section for hydrogen (Ref. 13) added to curve (II); (IV) coherent scattering, using form factors for the entire water molecule (Ref. 14); (V) coherent scattering, using form factors from diffraction experiments (Ref. 16); (VI) incoherent scattering, calculated as the sum of the oxygen plus twice the hydrogen differential cross sections, corrected for electron binding with the use of incoherent scattering form factors (Ref. 13).

$$r_e = e^2/(4\pi\epsilon_0 m_e c^2)$$

is the classical radius of the electron, e the electron charge, ϵ_0 the permittivity of free space, m_e the electron mass, and c the speed of light. If interelectron interference were ignored, $d\sigma_{\mathrm{coh}}(\theta)/d\Omega$ for water would be $10\, d\sigma_T(\theta)/d\Omega$, shown as curve (I) in Fig. 2 for scattering angles between 0° and 30°.

$F_{\mathrm{coh}}(s, \rho_e(\mathbf{r}))$ is dependent upon $\rho_e(\mathbf{r})$, the statistical spatial distribution of the electrons, and upon s, defined[12] as

$$s = \frac{E}{hc}\sin(\theta/2), \tag{4}$$

where E and h are the photon energy and Planck's constant, respectively. Since the photon does not change energy in coherent scattering, the product $2hs$ is the change of momentum of the photon.

For a given material, the form factor may be evaluated at three levels of complexity, depending on the extent of the interelectron interference considered. One may (a) consider only the interference between scatterings from electrons in the same atom, (b) include also the interference between electrons of different atoms belonging to the same molecule, and (c) take into account the additional effects of interference between molecules.

For water, since the major component of the molecule is the oxygen atom, the first level of analysis is to consider scattering only from oxygen. Using the values of

$$F_{\text{coh}}\,(s, \rho_e(\mathbf{r})|_{\text{O}})$$

tabulated by Hubbell *et al.*,[13] at 60 keV we obtain the differential cross section shown as curve (II) of Fig. 2. If scatterings from the hydrogen atoms are considered, but the effects of interference between electrons of different atoms in the molecule are not included, we obtain curve (III). This is evaluated as

$$\{2[F_{\text{coh}}(s, \rho_e(\mathbf{r})|_{\text{H}})]^2 + [F_{\text{coh}}(s, \rho_e(\mathbf{r})|_{\text{O}})]^2\}\, d\sigma_T\,(\theta)/d\Omega\,.$$

This differential cross section, however, is only slightly greater than that shown as curve (II), since at $\theta = 0°$ the scattering cross section for an isolated hydrogen atom is only 1/64th that of an oxygen atom.

At the next level of complexity, when the interference between all ten electrons is accounted for by calculating a form factor[14] based on the statistical distribution $\rho_e(\mathbf{r})|_{\text{H}_2\text{O}}$ of the electrons in the water molecule as a whole, there is a significant increase in the low-angle scattering probability [curve (IV)].

The third, most rigorous, approach requires taking into account the coherence between electrons belonging to different molecules. The appropriate form factor can, in theory, be calculated from an electron distribution $\rho_e(\mathbf{r})|_{\text{liquid water}}$ which is the convolution of the distribution of electrons within individual molecules with the distribution of the position and orientation of the molecules relative to one another. For many materials, however, this distribution is not known. Information about the material's molecular structure can be extracted from x-ray diffraction data by comparing with the calculated scattering distribution from free molecules. Such a structural study for liquid water, performed with Mo Kα radiation (17.44 keV), was reported by Narten *et al.*[15–17] Scattering form factors at a number of temperatures, obtained for $0.016 \leqslant s \leqslant 12.7$ nm^{-1}, and extrapolated to $s = 0$ nm^{-1}, were tabulated in Ref. 16, with details on the experimental procedure documented in Ref. 17. Using Eqs. (2), (3), and (4), we have calculated from their data values of $d\sigma_{\text{coh}}\,(\theta)/d\Omega$ at the energies used in radiology.[18]

At energies higher than 17.44 keV, values of s larger than those for which Narten's group performed their measurements are possible. Since at large s the diffraction data converge upon the curve for free oxygen atoms, we have used form factors from Hubbel *et al.*[13] for oxygen when $s > 12.7$ nm^{-1}.

The dependence of F_{coh} on s varies only slightly between the diffraction data obtained at 20, 25, and 50 °C. The corresponding total cross sections, integrated over all solid angles, differ from each other by less than 5% at all energies between 15 and 150 keV. We have used the data at 25 °C.

The resulting differential scattering cross section for liquid water at 60 keV is shown in Fig. 2 as curve (V). The effect of intermolecular coherence is seen to be an oscillation around curve (IV) for a free molecule. The greatest effect is for scattering near $\theta = 0°$, for which there is almost complete destructive interference. This is a well-known effect seen in diffraction studies on amorphous substances such as water.[19,20] The scattering probability has a maximum at a nonzero scattering angle. At 60 keV, this occurs at 3.8° (Fig. 2); it occurs at 11.3° for 20 keV and 2.2° for 100 keV. Although these data were obtained for pure water, we expect the differential cross section for the water in cells to be qualitatively similar, that is, having an oscillation about the free-molecule curve with a maximum at $\theta > 0°$.

TABLE I. Integrated cross sections for coherent scattering.

Photon energy, keV	Cross section, 10^{-24} cm^2/molecule: Free O atom + 2 free H atoms[a]	Free H_2O molecule[b]	Liquid water[c]
15	3.98	4.47	3.66
20	2.65	2.92	2.46
30	1.40	1.52	1.32
40	0.861	0.931	0.815
60	0.417	0.444	0.392
100	0.161	0.170	0.151
150	0.0733	0.0774	0.0691

[a] Calculated using form factors given by Hubbell *et al.* (Ref. 13).
[b] Calculated using form factors calculated by Blum (Ref. 14).
[c] Calculated from liquid water diffraction data reported by Narten (Ref. 16).

It should be noted that if the material is not amorphous, the differential cross section depends upon the azimuthal angle as well as upon θ. Thus, diffraction spots from metal beam filters can be observed if the grain size of the metal is in the appropriate range.[21]

The total interaction cross section, obtained by integrating the diffraction data differential cross section over 4π steradians, is shown in Fig. 1. It should be noted that although the differential cross section for small θ is quite sensitive to the method of obtaining F_{coh}, the integrated cross section is not. Over the energy range 15–150 keV, the total coherent cross section, calculated assuming independence between the O and H atoms, is within 9% of that calculated from the diffraction data (Table I). Moreover, these differences in the coherent cross section lead to differences of less than 1% in the total interaction cross section, i.e., the sum of the coherent, incoherent, and photoelectric probabilities.

B. Incoherent scattering

For inelastic scattering, each electron contributes independently to the total scattering probability. The cross section for water was calculated as

$$d\sigma_{\text{incoh}}(\theta)/d\Omega = \{2F_{\text{incoh}}(s, Z = 1) + F_{\text{incoh}}(s, Z = 8)\} \times [C_{\text{KN}}\, d\sigma_T(\theta)/d\Omega\,], \quad (5)$$

where C_{KN} is the energy-dependent part of the Klein–Nishina differential cross section, which is contained in the square brackets of Eq. (5). The $F_{\text{incoh}}\,(s,Z)$ are incoherent scattering form factors which correct for the electron binding energies; we used the values tabulated by Hubbell *et al.*[13]

The resulting differential cross section at 60 keV is given as curve (VI) in Fig. 2. The form factors reduce the scattering probability in the forward direction, where the energy transferred to the electron is of the same order of magnitude as the binding energy.

The incoherent scattering cross section, integrated over

all angles, is shown in Fig. 1. It decreases below 35 keV because of the binding energy correction. For energies used in diagnostic radiology other than for mammography, the total probability for incoherent scattering is much greater than that for coherent scattering. Figure 2 shows that at small scattering angles, however, coherent scattering predominates. At 60 keV, it is over 8 times more probable than incoherent for $\theta = 5°$.

IV. MEASUREMENTS OF TOTAL SCATTER

To compare the calculated values of $S_{1,coh}/P$ in imaging systems with S_{tot}/P, the ratio of the total scattered energy fluence to primary, the latter was determined using the experimental configuration shown in Fig. 3. A Plexiglas tank 25-cm square containing water was positioned with its bottom 93.3 cm from the focal spot of a General Electric Model 11DB4 rotating anode tube driven by a single-phase generator. A scintillation detector, consisting of a 2-mm-thick bismuth germanate crystal coupled via a light pipe to a photomultiplier tube (PMT), was located beneath the phantom. The air gap between the phantom exit and the detector was variable. A grid could be inserted between the phantom and detector, with its midplane 5 cm from the phantom exit.

S_{tot}/P was determined using a modification of the method developed by Wilsey.[23] First, a measurement was made with the primary stopped by a 3-mm-thick Pb blocker placed above the phantom on a Styrofoam support (not shown). The total radiation fluence was then measured with the blocker removed, allowing calculation of S_{tot}/P. Measurements were performed by integrating the charge produced by the PMT on an electrometer. Each measurement was corrected for fluctuations in x-ray tube output by normalizing to the output of an ionization chamber positioned beneath the x-ray tube collimator.

Since off-focal radiation, and x rays scattered by the filters and collimator, could pass around the Pb blocker and be confused with scatter, the method of Yaffe *et al.*[24] was used to correct for this as follows. With the phantom removed, two additional measurements were made, one with the Pb blocker of the spurious source radiation, and one without the blocker of the total radiation. Using all four measurements, the primary transmission through the phantom and the amount of the unwanted radiation reaching the detector with the phantom present were calculated.

Since the blocker shadows the phantom, it reduces the scattered fluence somewhat. To correct for this, the above procedure was carried out for each experimental point using three blockers of different area, and $S_{tot}/(S_{tot} + P)$ was extrapolated to zero blocker area. Similar extrapolation methods have been used by others.[11,25]

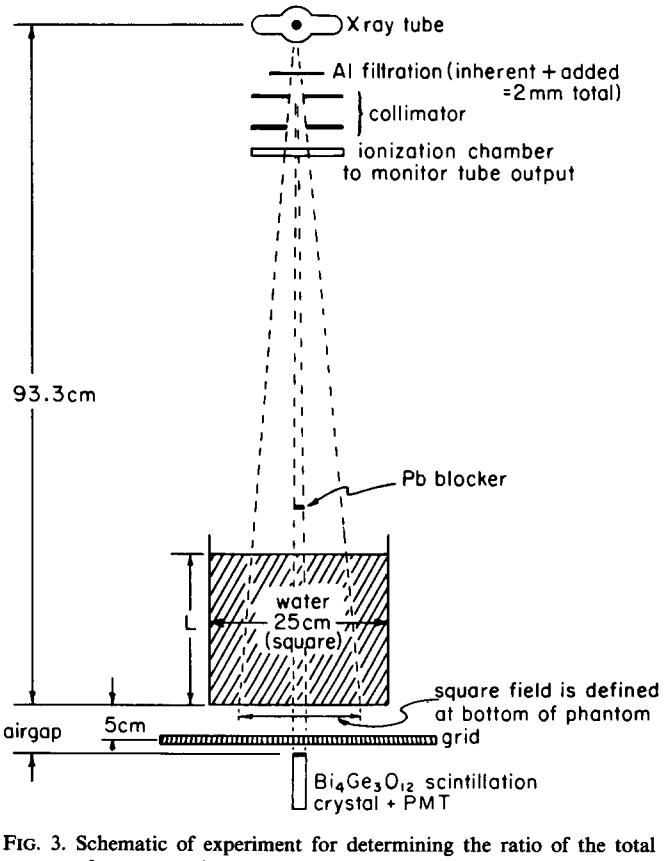

FIG. 3. Schematic of experiment for determining the ratio of the total amount of scatter to primary S_{tot}/P. The Pb primary blocker is located on a Styrofoam support (not shown).

V. RESULTS

A. Dependence on field size, air gap, and phantom thickness

Results of our experiments and calculations for an 80-kVp beam without a grid are shown in Figs. 4, 5, and 6. In each figure, the upper curve is the experimentally determined value of S_{tot}/P, the lowest curve is the calculated value of $S_{1,coh}/P$, and the middle curve is the ratio of the sum of coherent plus incoherent first scatter to primary $(S_{1,coh} + S_{1,incoh})/P$. The difference between the top and middle curves is the multiple scatter component.

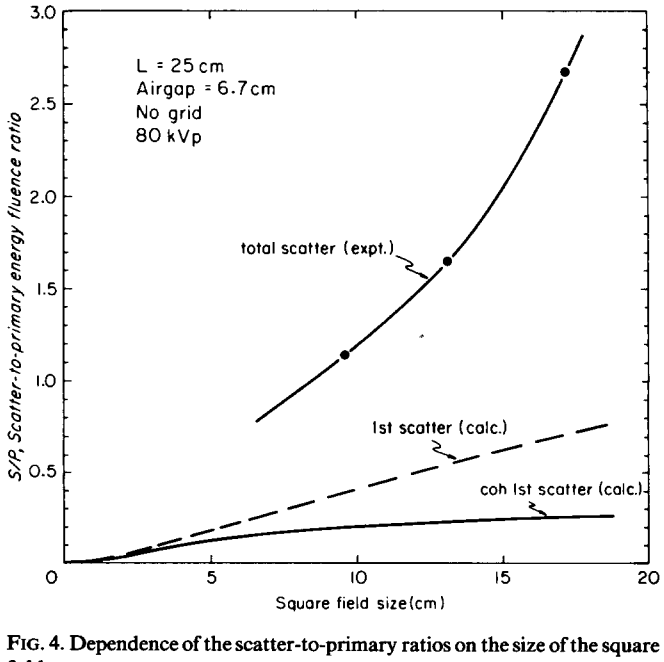

FIG. 4. Dependence of the scatter-to-primary ratios on the size of the square field.

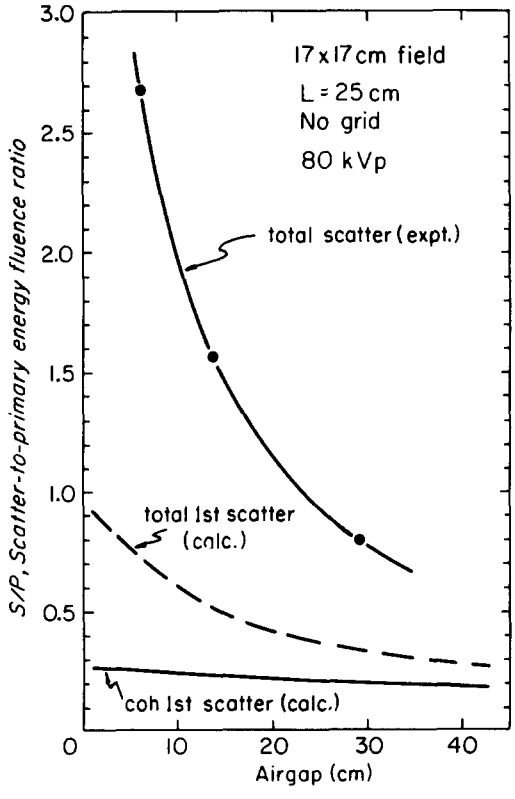

FIG. 5. Dependence of the scatter-to-primary ratios on air gap.

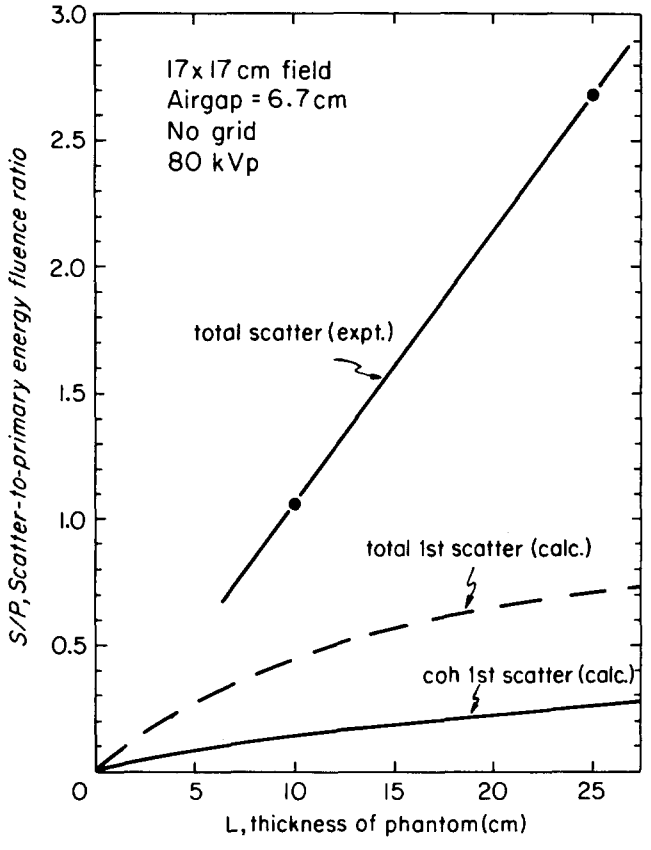

FIG. 6. Dependence of the scatter-to-primary ratios on the phantom thickness L.

Figure 4 shows that $S_{1,coh}/P$ approaches a constant value with increasing field size. This occurs because coherent scatter is probable only at low angles, so that the scatter reaching the detector arises mainly from the central area of the phantom. In contrast, the angular distribution of incoherent first scatter is broader, and therefore $S_{1,incoh}/P$ continues to grow with field size. S_{tot}/P increases supralinearly with field size because of the rapid increase of multiple scatter.

In Fig. 5 the air gap was varied. Both S_{tot}/P and $S_{1,incoh}/P$ fall off rapidly with increasing air gap, while $S_{1,coh}/P$ decreases slowly. For a given scattering site the solid angle $d\Omega/da$ subtended by a unit area of the detector decreases as the air gap is increased. The angle θ for single scattering to the detector, however, is also decreased, resulting in an increase in $d\sigma_{coh}(\theta)/d\Omega$ for most of the scatter sites. This offsets to a large measure the effect of the decrease in $d\Omega/da$.

The dependence on phanton thickness is shown in Fig. 6. Both $S_{1,coh}/P$ and $S_{1,incoh}/P$ grow sublinearly. Consider the phantom to be composed of layers of material. When an additional layer is added, the contribution made by the original layers to the ratio of first scatter to primary at the detector is unchanged, since both are reduced by the same factor. Single scatter from the added layer, which is further from the detector, contributes a lesser amount to the ratio for two reasons. First, $d\Omega/da$ is reduced, and second, the ratio of the transmission of the scatter T_{Si} to the transmission of primary from the layer containing the scattering site to the detector is generally less than for the deeper layers, because photons first scattered at $\theta \neq 0°$ follow a longer path than the primary, the additional path length increasing with distance from the detector. In the case of coherent first scatter, this is partially compensated by an increase in the number of scatter sites for which $d\sigma_{coh}(\theta)/d\Omega$ is large, with the result that $S_{1,coh}/P$ grows more quickly with phantom thickness than does $S_{1,incoh}/P$, although still sublinearly.

B. Reduction of $S_{1,coh}/P$ by antiscatter mechanisms

1. Large air gaps

For some examinations, particularly chest radiography, a large air gap is used to allow the scatter to diverge from the primary and miss the image receptor. As discussed in the previous section (Fig. 5), however, $S_{1,coh}/P$ decreases only slowly with increasing air gap. The large air gap favors the detection of low angle as opposed to large-angle scatter so that much of the remaining scatter contamination of the image is due to coherent first scatter.

2. Grids

Grids are usually used in conjunction with small air gaps. From Fig. 5, for conditions representative of an abdominal examination—17×17 cm field, 25 cm of water, 6.7-cm air gap—without a grid the total amount of scatter is 2.7 times primary. Coherent first scatter comprises 10% of this. In a separate experiment with a 12:1 grid in place, S_{tot}/P was found to be 0.34.

To determine how much of the scatter behind the grid is first coherent, we must consider how the grid removes the different types of scatter. Figure 7(a) shows the distribution

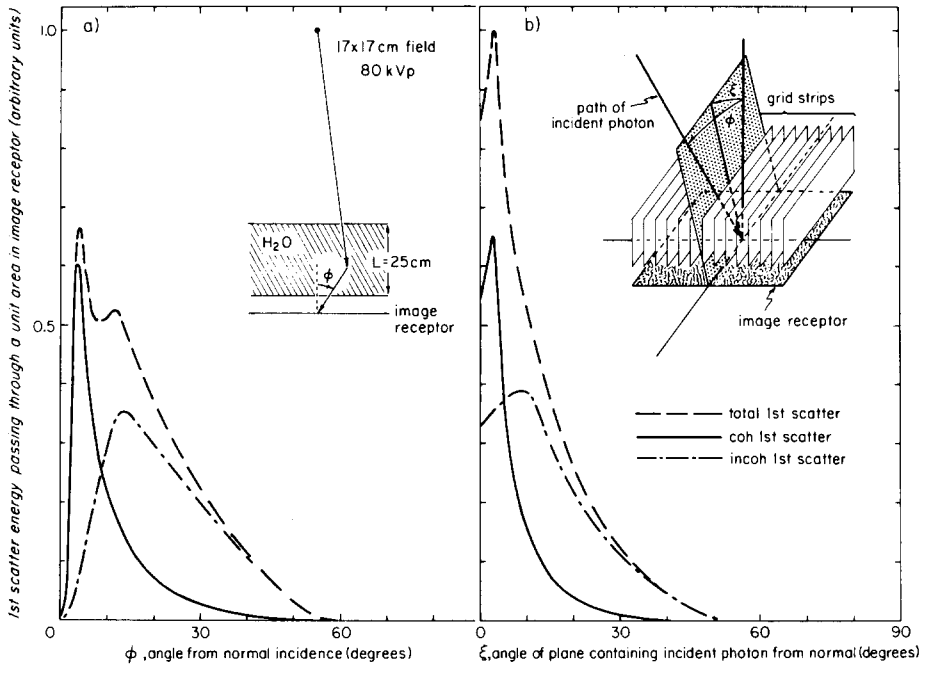

FIG. 7. Angular distributions of first scatter approaching the image plane. (a) Distribution versus the angle from normal incidence. (b) Distribution versus the angle of inclination of the plane containing both the incident photon path and the direction of the grid strips.

of the two types of single scatter approaching the center of the image receptor versus ϕ the angle from the normal incidence. The coherent first scatter is peaked at an angle of less than 5°, while the incoherent first scatter is spread out over a much larger range of ϕ. We expect, therefore, that grids will be less effective in dealing with coherent first scatter than with incoherent or multiple scatter.

Since grids are composed of linear Pb strips, in order to make a quantitative assessment of their performance, we have shown in Fig. 7(b) the distribution of first scatter versus ξ the angle of inclination of the plane containing both the direction of the grid strips and the path of the incident photon. Since we do not know the exact distribution of the multiple scatter in ξ, we estimated a distribution by assuming that the multiple scatter emerging from a given point on the phantom exit is isotropic, and that the intensity falls off with distance from the beam centerline. Measurements of radiation transmission versus ξ for various grids have been published by Dick and Motz.[26] Since the first-scattered energy fluence spectrum arising from the phantom for 80 kVp has a mean energy of about 59 keV, we used the average of their measured transmission values at 49 and 69 keV as an approximate value for the transmission of our scatter spectrum. By calculating the amount of scatter transmitted at each ξ and summing over ξ, it was determined that behind the grid coherent first scatter accounts for approximately 22% of the scatter present.

C. Amount of coherent first scatter in diagnostic examinations

Table II summarizes scatter-to-primary ratios for various diagnostic examinations. The values for an abdominal examination were taken from the previous section. For chest

TABLE II. Scatter-to-primary ratios in diagnostic examinations.

		Phantom thickness cm	Phantom material	Field size cm	Antiscatter mechanism	$\frac{S_{tot}}{P}$ (expt.)	$\frac{S_{1,coh}}{P}$ (calc.)	$\frac{S_{1,coh}}{S_{tot}}$	
Chest	120 kVp	13	H_2O	30×30	large air gap	2.3[a]	0.12	0.05	6.7 cm air gap
						1.2[a]	0.11	0.09	20 cm air gap
Abdomen	80 kVp	25	H_2O	17×17	12:1 grid	2.7	0.26	0.10	before grid
						0.34	0.075	0.22	after grid
Mammography	30 kVp (Mo)	4.5	Lucite	12-cm circular	none	0.6[b]	0.24	0.4	
CT—body	120 kVp	30-cm-diam cylinder	H_2O	0.6-cm slice	Postpatient collimation against out-of-slice scatter	0.052[c]	0.012[c]	0.23	

[a] Estimated for 120 kVp from the data of Stargardt and Angerstein (Ref. 28) which span 60–105 kVp; above 95 kVp, the energy dependence is negligible.
[b] Obtained by interpolating the data of Barnes and Brezovich (Ref. 11) in phantom thickness and field size.
[c] Calculated from Johns and Yaffe (Ref. 30).

radiography and mammography, we have calculated $S_{1,coh}/P$ and compared with experimentally determined values of S_{tot}/P published by others.

For chest radiography, Niklason *et al.*[27] have shown that S_{tot}/P varies widely across the image because of the variations of the transmission of primary and scatter through the different regions of the thorax. The values shown here in Table II are for a simplified phantom which is homogeneous and of uniform thickness. Comparing our values of $S_{1,coh}/P$ with values of S_{tot}/P estimated from the measurements of Stargardt and Angerstein,[28] we find that even at the energies used in chest radiography, when a large air gap is used, coherent scatter is on the order of 10% of both the primary and the total scatter reaching the image receptor.

For mammography, in order to compare to the measurements of Barnes and Brezovich[11] for Lucite phantoms, we calculated $S_{1,coh}/P$ for Lucite using form factors from Hubbell *et al.*,[13] ignoring interatomic interference effects. As expected from Fig. 1, the magnitude of coherent scatter is greatest at these low energies: 24% of primary and 40% of all scatter. We expect, however, that grids, which have recently been developed for mammography,[29] will be more effective at removing coherent first scatter in mammography than in higher energy examinations, because $d\sigma_{coh}(\theta)/d\Omega$ is peaked at greater angles (11.3° at 20 keV versus 3.8° at 60 keV).

Also shown in Table II are values for a fourth-generation CT scanner in which the detectors are 90 cm from the phantom center. A postpatient collimator against scatter arising from outside the primary slice was assumed to remove 40% of total scatter. S_{tot}/P for a 30-cm-diam phantom was calculated from Eq. (8) of our previous communication[30] to be about 5%. Using the value of $S_{1,coh}/P$ obtained from Fig. 2 of that work, coherent first scatter is found to make up 23% of total scatter. This large fraction is due to the use of a large air gap and collimation against multiple scatter. In third-generation scanners, where the detectors are collimated against scatter arising from within the slice, S_{tot}/P is less, but an even higher proportion of the total scatter is first coherent.

VI. EFFECT OF COHERENT FIRST SCATTER ON RADIOGRAPHIC IMAGES

Having determined the amount of coherent scatter present in diagnostic images, we now consider its effect on image quality. The effect of a scattered photon depends on the photon's displacement from the primary path at the image plane. If the displacement is zero, there will be no effect on the image; if the displacement is several millimeters or more, there will be a reduction of broad-area contrast. Intermediate displacements are considered to result in loss of resolution.

The differential cross section for scattering towards a unit area in the image plane is

$$\frac{d\sigma}{da}(r,x) = \left[\frac{1}{x^2(1+r^2/x^2)^{3/2}}\right]\frac{d\sigma}{d\Omega}(\theta) \times \frac{10^{-24}\ \text{cm}^2}{\text{molecule—cm}^2\ \text{of image}}, \quad (6)$$

where r is the distance from the primary path and x is the perpendicular distance from the scattering site to the image receptor. The factor in square brackets is $d\Omega/da$, the solid angle subtended at the scattering site by the unit area in the image plane. Figure 8 shows the dependence of $d\sigma/da$ on r/x for coherent, incoherent, and total first scatter. The curves have been multiplied by x^2 to remove the dependence on the distance from the scattering site to the image plane. These distributions may be thought of as point spread functions for scattering from a single site, disregarding attenuation.

The primary ray intersects the image plane at $r/x = 0$, at which point the incoherent scatter distribution falls to zero because of electron binding. In this region, the coherent distribution also has a minimum because of destructive interference. Near the primary ray, the shape of the total first-scatter distribution is mainly determined by the coherent component. As the photon energy is increased, the coherent distribution becomes narrower, but even at 100 keV the full width at half maximum for an image receptor at $x = 10$ cm is 1.25 cm.

The insets to the graphs for 40 and 60 keV show the Fourier transforms of the distributions. The coherent distribution contains frequencies much higher than those of the incoherent. For example, at 60 keV with $x = 10$ cm, the first zero of the coherent frequency distribution is at 0.029 cycles/mm, versus only 0.006 cycles/mm for the incoherent distribution. The coherent distribution has significant magnitude well beyond its first zero; however, it does not exceed 5% of the zero-frequency value for total first scatter for frequencies above 0.14 cycles/mm. These frequencies are too low to give rise to objectionable structure in a radiograph. Rather, we conclude that coherent first scatter has the same effect as other types of scatter: a semiuniform fog across the image which decreases contrast and SNR.

VII. EXPERIMENTAL VERIFICATION

The results of Sec. V were based on a numerical integration of the contribution made by each scattering volume in the phantom to the first-scatter fluence at the image receptor. Although it would be desirable to verify our results by experiment, no practical method is apparent for distinguishing coherent first scatter from primary, incoherent first scatter, or multiple scatter on the basis of either direction or energy[31] for such geometries.

We can, however, distinguish coherent scatter from primary on the basis of direction if a very narrow primary beam is employed. In addition, the use of a thin phantom ensures that first scatter predominates over multiple scatter, allowing comparison between calculation and experiment.

A pencil beam of primary radiation was produced by collimating the output of a Machlett Aeromax 516-CL 1510 stationary anode tube with two 0.7 mm Pb apertures (Fig. 9). The tube was run at 80 kVcp with 2.6-mm Al filtration. A water sample in a plastic container measuring $2.2 \times 3.9 \times 7.5$ cm was placed behind the second aperture. Since the volume of water irradiated by primary was only about 0.01 cm^3, the intensity of scatter was very low compared to primary. To image the scatter we used a sheet of Kodak No-Screen film (type NS-5T), placed in a light-tight box. Cassettes and flu-

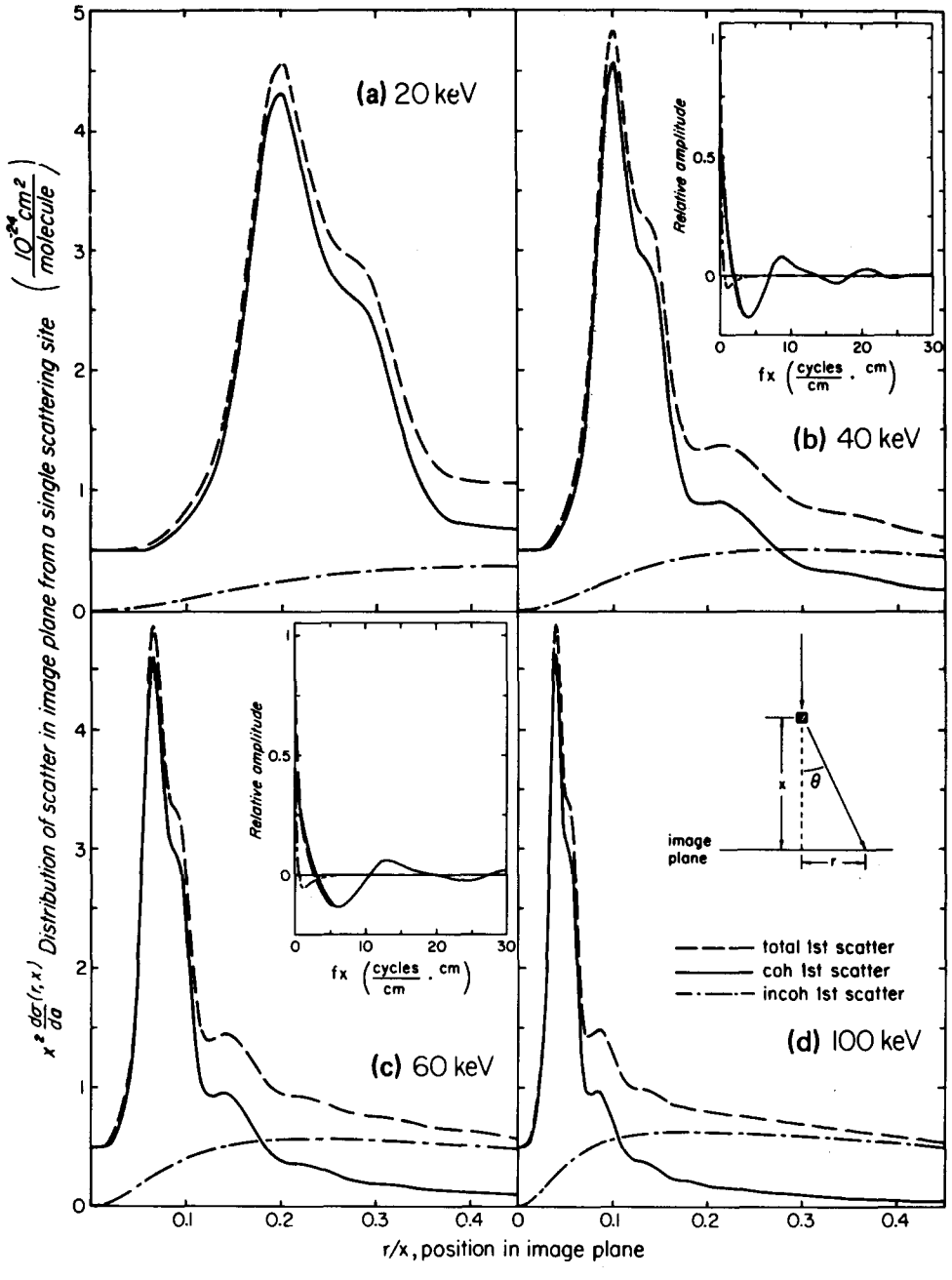

FIG. 8. Distributions of first scatter in the image plane from a single scattering site, for incident photon energies of (a) 20 keV, (b) 40 keV, (c) 60 keV, and (d) 100 keV. To remove the dependence on the distance x from the scattering site to the image plane, the curves have been multiplied by x^2. The insets of (b) and (c) are the Fourier transforms of the spatial distributions. Their abscissas should be divided by x to obtain spatial frequencies f in the image plane.

orescent screens were avoided to minimize the production of extraneous scatter which would contaminate the image. Furthermore, black paper was used to construct the entrance and exit windows of the box. Only about 1% of the incident x-ray fluence interacts with these windows.

A sensitometry scale was produced for each image by exposing a strip cut from the same sheet of film to the primary beam for several different times at reduced tube current. The sensitometry strip and its image film were manually processed together; thus effects due to variations in processing speed were circumvented. With direct x-ray exposure the sensitometric properties of the film are not affected by reciprocity law failure.[32] We confirmed that under our conditions latent image fading led to a loss of only about 3% of image intensity, and therefore could be ignored. Hence, with

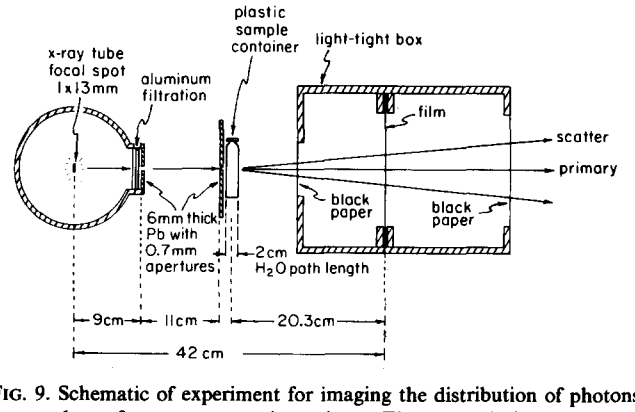

FIG. 9. Schematic of experiment for imaging the distribution of photons scattered out of a very narrow primary beam. The x-ray tube has 2.6-mm Al total of inherent plus added filtration. The entrance and exit walls of the sample container are each 1-mm thick.

the use of the sensitometry scales, quantitative information could be obtained from our images.

Figure 10 shows representative films from the experiments. Figure 10(a),a short exposure with no water sample, shows the primary beam. Although it is not evident on the reproduction of the radiograph, the primary consists of a 0.7-mm-diam region of central blackening surrounded by collimator penumbra for a total diameter of about 2 mm at the film plane. Figure 10(b) is a 6-h exposure of the primary transmitted through an empty sample container. The blackened area of the film is greater than in Fig. 10(a) because of internal scattering within the film. There is also a small amount of film blackening, not readily visible, over a larger region due to scattering from the plastic container. Localized areas of darkening away from the primary beam, two of which are indicated by arrows, are diffraction spots from the Pb aperture. Figure 10(c) is a 6-h exposure with the sample container filled with water. The region of primary blackening is smaller than in Fig. 10(b) because of attenuation in the sample. Radiation that has been coherently scattered in the sample is visible as a halo or "smoke ring" of about 4-cm diameter. This somewhat startling effect is due to destructive interference at small scattering angles, as discussed pre-

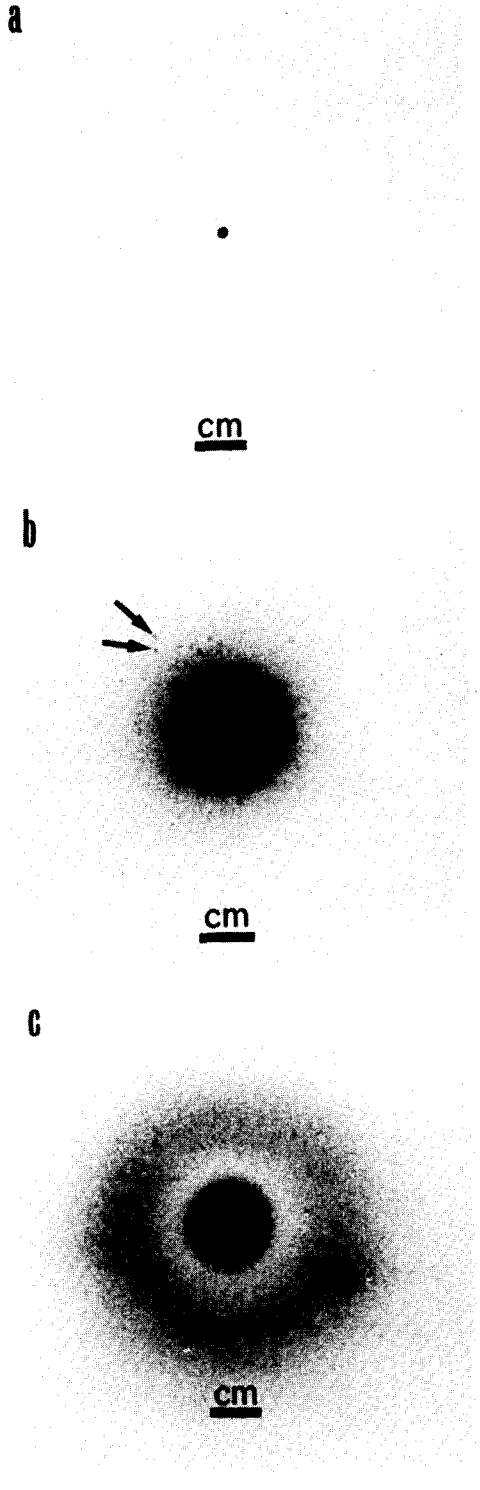

FIG. 10. Films obtained with the setup shown in Fig. 9. (a) Short exposure without the sample in place showing the primary beam and its penumbra. (b) Long exposure [~30 000 times the x-ray fluence of (a)] with an empty plastic sample container in the beam. The arrows indicate two of the diffraction spots from the Pb primary aperture adjacent to the container. (c) Long exposure [same as (b)] with the sample of water in place, showing the halo or "smoke ring" due to scatter. The region of primary blackening is smaller than in (b) because of sample attenuation.

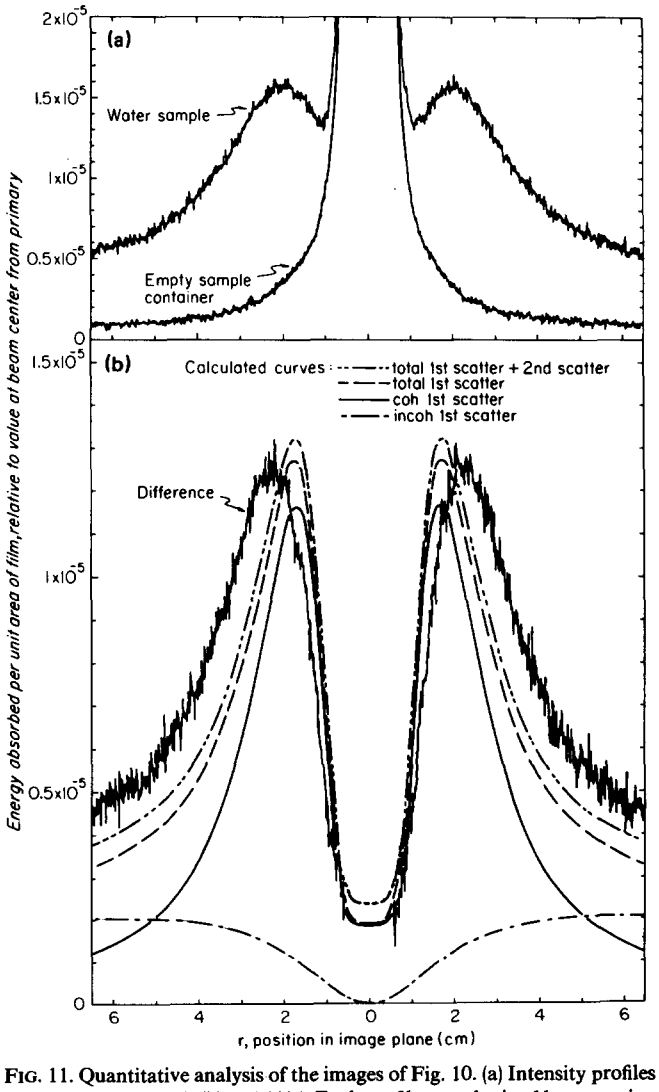

FIG. 11. Quantitative analysis of the images of Fig. 10. (a) Intensity profiles across films of Figs. 10(b) and 10(c). Each profile was obtained by averaging 12 microdensitometer scans and applying sensitometry to obtain intensities relative to that of the primary at beam center. The curve for the empty sample container has been multiplied by 0.603, the measured transmission of the primary through the water. (b) Difference of the two intensity profiles shown in (a), compared with calculated scatter distributions.

viously in Secs. III and VI. While this result was obtained with a sample of pure water, a film displaying a similar halo was obtained with a sample of sirloin steak, and a film with a slightly smaller diameter halo was obtained with a 4-M NaCl solution. We expect, therefore, that a similar distribution of scatter would be produced by the water in living tissue. We noted that no such ring was seen when using a Lucite plate, suggesting a more random distribution of atomic positions.

To quantify these results, the images of Figs. 10(b) and 10(c) and their corresponding sensitometry strips were scanned by a Perkin Elmer PDS digitizing microdensitometer using a 125-μm square sampling aperture. Twelve diametrical scans were made of each image. The densities were averaged and converted to x-ray intensity. These are shown in Fig. 11(a). The profile from the film with the empty container has been multiplied by 0.603, the measured transmission of primary energy through the sample, and thus the width of the base of the intense area of film blackening has been reduced to that of the film with the water present. This represents the profile that would result from only the primary transmitted through the water sample.

When this profile is subtracted from that with the water present, we obtain the distribution of Fig. 11(b). Also shown are distributions of the ratios of the coherent first-, incoherent first-, and total first-scatter fluences to the primary at the beam centerline, calculated by the method of Sec. II. Since the volume irradiated by primary is compact, these distributions, calculated for an 80-kV spectrum, are essentially weighted averages of distributions such as those shown in Fig. 8 for scattering of monoenergetic photons from a single site.

In addition to the first-scatter calculations, an estimate of the amount of multiple scatter present was made by calculating the second-scattered fluence reaching the detector using the method of Wong *et al.*[33] The second-scattered fluence was found to be fairly uniform with position, and the value at beam center was therefore assumed to apply at all positions. This multiple scatter contribution could have been reduced if a sample container smaller in lateral extent had been used.

Since the area of the x-ray tube focal spot is considerably larger than those of the primary beam apertures, the beam had a trapezoidal profile at the film plane. The first- and second-scatter calculations were corrected for this effect to allow proper comparison with the experimental results.

Comparing the measured intensity profile with the calculated curve for total first plus second scatter, we see that both the magnitude and shape are in reasonable agreement. The peak of the experimentally determined distribution is within about 6% of that of the calculated curve which includes second scatter. The distribution from experiment peaks at a slightly larger radius than does the calculated curve. This may be due, in part, to errors incurred when taking the difference between the two distributions of Fig. 11(a) near the primary beam, where both have large values.

VIII. CONCLUSIONS

From this study of coherent first scatter in diagnostic radiology, we draw the following conclusions:

(1) The forward-peaked nature of coherent scatter compensates for its small interaction cross section, and hence the amount of coherent first scatter reaching the image receptor is comparable to the amount of incoherent first scatter.

(2) Coherent scatter comprises a significant fraction of the *total* scatter reaching the image receptor. For conditions representative of those encountered in radiography of the abdomen, namely 80 kVp, a 17×17 cm field and a 25-cm-thick water phantom, 10% of the scatter before a grid, and on the order of 22% behind a 12:1 grid is coherent first scatter. The fraction is reduced for higher kVp examinations, and increased for examinations done with lower x-ray energy, such as mammography.

(3) The magnitude of coherent first scatter is significant compared to that of primary. For an abdominal examination, $S_{1,\mathrm{coh}}/P$ is 26% before a grid, and 7.5% after a 12:1 grid.

(4) Coherently scattered photons diverge far enough from the primary ray to add a semiuniform fog to the image, as do other types of scatter. For a scattering site 10 cm from the image plane, the value of the spatial frequency distribution of coherent first scatter does not exceed 5% of the zero-frequency value for total first scatter for frequencies above 0.14 cycles/mm. Hence, coherent scatter does not generate discernable structure on a radiograph, but decreases contrast and SNR.

(5) Since coherent first scatter does not diverge as far from the primary as do other types of scatter, especially at higher energies, it is more difficult to remove from images. Grids and large air gaps are less effective in reducing the ratio of coherent first scatter to primary than they are in reducing the ratios of incoherent and multiple scatter to primary.

(6) In this work, we used experimentally determined[16] form factors for coherent scattering from liquid water. The resulting differential cross sections are reduced almost to zero for angles near 0° because of destructive interference between scatterings from electrons of different molecules. The scattering probability has a maximum at a nonzero angle which depends on photon energy. The maximum is at 11° for 20 keV and at 2° for 100 keV. Consequently, coherent scattering from a single interaction site results in a ring-shaped distribution of photons at the image receptor.

ACKNOWLEDGMENTS

We are grateful to Dr. J. Cunningham and J. Wong for discussions and suggestions regarding this work. This study was supported by the National Cancer Institute of Canada, Physicians Services Inc. Foundation, and the Ontario Cancer Treatment and Research Foundation. The first author acknowledges the assistance of the Medical Research Council of Canada.

[1] K. G. Strid, Acta Radiol. Oncol. **19**, 129 (1980).
[2] S. A. Kerr, K. Kouris, C. E. Webber, and T. J. Kennett, Phys. Med. Biol. **25**, 1037 (1980).
[3] J. T. Stalp and R. B. Mazess, Med. Phys. **7**, 723 (1980).
[4] H. Olkkonen, P. Puumalainen, P. Karjalainen, and E. M. Alhava, Invest. Radiol. **16**, 491 (1981).
[5] K. H. Reiss and B. Steinle, Phys. Med. Biol. **18**, 746 (1973). The full results are available from Siemens AG, UB Med, Henkestrasse 127, D-8520 Er-

langen, W. Germany as *Tabellen zur Röntgendiagnostik II*.
[6]N. Nakamori and H. Kanamori, abstract from V International Conference on Medical Physics, held in conjunction with the XII International Conference on Medical and Biological Engineering, Jerusalem, Israel, August 19–24, 1979.
[7]W. Kalender, Phys. Med. Biol. **26**, 835 (1981).
[8]R. Birch, M. Marshall, and G. M. Ardran, *Catalogue of Spectral Data for Diagnostic X-rays* (Hospital Physicists' Association, London, 1979).
[9]ICRP Report No. 23, *Report of the Task Group on Reference Man* (Pergamon, Oxford, 1975).
[10]D. R. White, R. J. Martin, and R. Darlison, Br. J. Radiol. **50**, 814 (1977).
[11]G. T. Barnes and I. A. Brezovich, Radiology **126**, 243 (1978).
[12]A variety of definitions of s are used in the literature. In addition to the definition given in Eq (4), $s = 4\pi(E/hc)\sin(\theta/2)$ and $s = 2(E/hc)\sin(\theta/2)$ are frequently used.
[13]J. H. Hubbell, W. J. Veigele, E. A. Briggs, R. T. Brown, D. T. Cromer, and R. J. Howerton, J. Phys. Chem. Ref. Data **4**, 471 (1975); **6**, 615 (E) (1977).
[14]L. Blum, J. Comput. Phys. **7**, 592 (1971).
[15]A. H. Narten and H. A. Levy, J. Chem. Phys. **55**, 2263 (1971).
[16]A. H. Narten, ORNL Report No. 4578 (1970).
[17]H. A. Levy, M. D. Danford, and A. H. Narten, ORNL Report No. 3960 (1966).
[18]F_{coh} depends on scattering angle and energy. At energies far from absorption edges, F_{coh} can be simply tabulated versus $s = (E/hc)\sin(\theta/2)$. Near absorption edges, resonance effects occur, and F_{coh} depends explicitly on E as well as on s (see Refs. 19 and 20). Since the energies used in medical imaging are far above the absorption edges for water, no corrections for resonance effects are required here.
[19]R. W. James, *The Crystalline State. Vol. II. The Optical Principles of the Diffraction of X-Rays*, edited by L. Bragg (Bell, London, 1962).
[20]A. Guinier, *X-Ray Diffraction* (Freeman, San Francisco, 1963).
[21]C. A. Carlsson, P. R. Edholm, and T. Ericsson, Med. Phys. **6**, 59 (1979).
[22]E. F. Plechaty, D. E. Cullen, and R. J. Howerton, LLL Report No. UCRL-50400, Vol. 6, Revision 1 (1975).
[23]R. B. Wilsey, Am. J. Roentgenol. **8**, 328 (1921).
[24]M. Yaffe, A. Fenster, and H. E. Johns, J. Comput. Assist. Tomogr. **1**, 419 (1977).
[25]A. E. Burgess and G. Pate, Med. Phys. **8**, 33 (1981).
[26]C. E. Dick and J. W. Motz, Med. Phys. **5**, 133 (1978).
[27]L. T. Niklason, J. A. Sorenson, and J. A. Nelson, Med. Phys. **8**, 677 (1981).
[28]A. Stargardt and W. Angerstein, Fortschr. Röntgenstr. **123**, 364 (1975).
[29]W. Lammers and H. Kuhn, Electromedica **1**, 2 (1979).
[30]P. C. Johns and M. Yaffe, Med. Phys. **9**, 231 (1982).
[31]Coherent and incoherent first scatter have almost identical energies at low scattering angles. For example, a 50-keV photon, incoherently scattered at 5°, loses only 0.02 keV of energy, and therefore cannot be distinguished experimentally from a 50-keV coherently scattered photon.
[32]J. F. Hamilton, in *The Theory of the Photographic Process*, 3rd ed., edited by C. E. K. Mees and T. H. James (Macmillan, New York, 1966), Chap. 10.
[33]J. W. Wong, R. M. Henkelman, A. Fenster, and H. E. Johns, Med. Phys. **8**, 775 (1981).